Magnetic, electrical, and GPR waterborne surveys of moraine deposits beneath a lake: A case history from Turin, Italy

GEOPHYSICS. VOL. 76, NO. 6 (NOVEMBER-DECEMBER 2011); P. B213–B224, 17 FIGS.
10.1190/GEO2011-0053.1

Case History

Magnetic, electrical, and GPR waterborne surveys of moraine deposits beneath a lake: A case history from Turin, Italy

Luigi Sambuelli[1], Cesare Comina[2], Silvia Bava[1], and Claudio Piatti[1]

ABSTRACT

Bathymetry and bottom sediment types of inland water basins provide meaningful information to estimate water reserves and possible connections between surface and groundwater. Waterborne geophysical surveys can be used to obtain several independent physical parameters to study the sediments. We explored the possibilities of retrieving information on both shallow and deep geological structures beneath a morainic lake by means of waterborne nonseismic methods. In this respect, we discuss simultaneous magnetic, electrical, and ground-penetrating radar (GPR) waterborne surveys on the Candia morainic lake in northerly Turin (Italy). We used waterborne GPR to obtain information on the bottom sediment and the bathymetry needed to constrain the magnetic and electrical inversions. We obtained a map of the total magnetic field (TMF) over the lake from which we computed a 2D constrained compact magnetic inversion for selected profiles, along with a laterally constrained inversion for one electrical profile. The magnetic survey detected some deep anomalous bodies within the subbottom moraine. The electrical profiles gave information on the more superficial layer of bottom sediments. We identify where the coarse morainic material outcrops from the bottom finer sediments from a correspondence between high GPR reflectivity, resistivity, and magnetic anomalies.

INTRODUCTION

This paper presents the results of different types of waterborne geophysical surveys carried out on a morainic lake in northern Italy. In this case study, we acquired geophysical information relevant to the bottom sediments and the underlying moraine in addition to the ones obtained in a previous study performed by the use of the ground-penetrating radar (GPR) (Sambuelli et al., 2010). The main objectives of this work were (1) increase the definition of a coarse grained water pathway in the lake sediments and (2) investigate in depth the moraine structure which emerges in the lake surroundings. The coarse-grain morainic material in this geologic setting likely contains boulders with magnetic signatures presenting a strong resistivity contrast with finer sediment type. Therefore, the survey techniques based on these two physical properties could be potentially useful. Moreover, the relatively shallow water depth in some areas of the lake and the aim to investigate also geological structures at depth below the lake sediments led us to a nonseismic approach, combining magnetic and electrical surveys with the GPR to constrain the interpretative models.

The use of nonseismic geophysical methods to study shallow inland water is relatively recent. A review of the existing methods and recent case histories can be found in the Special Issue of Near Surface Geophysics on Waterborne Geophysics (Butler, 2009; Sambuelli and Butler, 2009).

Applications of GPR to freshwater environments for both bathymetry estimation and bottom sediment characterization range from the initial investigations (Annan and Davis, 1977; Delaney et al., 1992; Arcone et al., 1992; Mellett, 1995; Moorman and Michel, 1997) to recent case histories (Arcone et al., 2006, 2010; Sambuelli et al., 2009, 2010; Lin et. al., 2010). Several of these authors stated

Manuscript received by the Editor 9 February 2011; revised manuscript received 6 June 2011; published online 6 January 2012.
[1]DITAG — Dipartimento di Ingegneria del Territorio, dell'Ambiente e delle Geotecnologie Politecnico di Torino C.so Duca degli Abruzzi, 24-10129 Turin, Italy. E-mail: luigi.sambuelli@polito.it; silviaquila@fastwebnet.it; claudio.piatti@polito.it.
[2]DST — Dipartimento di Scienze della Terra Università di Torino Via Valperga Caluso, 35-10125 Turin, Italy. E-mail: cesare.comina@unito.it.

that GPR surveys complement conventional sonic and ultrasonic approaches, especially in shallow water environments, or when the presence of gas prevents penetration of acoustic waves into the sediments. In particular, Arcone et al. (2010) discuss a GPR survey of a lake in a glacial environment (similar to our geological setting) and also give an example of the intrusion of moraine material through the lacustrine sediments.

The reported use of electric measurements on inland waters is more common than that of GPR, even though continuous vertical electric sounding (CVES) acquisition is relatively recent with the introduction of automatic multichannel resistivity devices. Electrical measurements have been applied for different purposes and using different configurations. To correctly choose the optimal acquisition array and electrodes disposition (floating or submerged) in relation to the objectives of our surveys, we have considered previous research works.

Lagabrielle and Teilhaud (1981) used a Wenner array on the Garonne River bottom to establish the extension of gravel deposits. Bradbury and Taylor (1984) studied the hydrogeological properties of the bottom sediments of Lake Michigan by combining seismic reflection and electrical measurements. They used a towed floating electrode array to yield longitudinal conductance and electrical chargeability measurements. Belaval et al. (2003) used continuous-resistivity profiling (CRP) to delineate the subsurface saltwater/freshwater interface by detecting conductivity changes in the marine environment. The CRP system was characterized by towing two fixed current electrodes and nine floating potential electrodes. They also used an echo sounder in their surveys to constrain the water depth during the inversion.

With respect to the use of submerged or floating electrode arrays, Loke and Lane (2004) compared the performances of three strategies to acquire resistivity data in water-covered areas: the first with a combination of underwater and floating electrodes of a Wenner array spaced at 2.5 m; the second with the entire survey line underwater with a minimum spacing between electrodes of 1 m, and the third with a floating dipole-dipole array with two fixed current electrodes and nine potential electrodes spaced at 10 m. Using numerical simulations, they found that floating electrodes reduced the subsurface depth of investigation.

Kwon et al. (2005) investigated the streamer resistivity survey method. They used floating and water bottom electrodes to find the minimum electrode spacing and thickness of the water layer which allows for the best results for different electrode configurations. Apostolopoulos et al. (2006) used Schlumberger and Pole-Pole electrode configurations to obtain information about the sedimentation characteristics under the sea bottom. Allen and Merrick (2007) analyzed the inversion of towed floating array datasets used for hydrogeological studies. They demonstrated that using a floating array with exponentially spaced potential electrodes provides the maximum depth resolution. Mansoor and Slater (2007) also used, for hydrogeological studies, 13 graphite floating electrodes tied from a paddleboat. They tested different electrode configurations, conventional and non conventional, and applied a modified Wenner-type array to maximize imaging based on theoretical sensitivity analysis of the modeled subsurface.

Geological information can be deduced from electrical measurements as demonstrated by Mitchell et al. (2008) using a towed, floating, equidistant electrode array to identify geologic heterogeneities causing the seepage from the bottom of a lake. Kelly et al. (2009) investigated the capability of towed floating electrical cable to map a known aquifer recharge zone and to provide hydrological information and electrical properties of the sediments. The electrical cable was 156 m long, with two current electrodes followed by nine potential electrodes using dipoles configuration as described by Allen and Merrick (Allen and Merrick, 2007). Slater et al. (2010) used both electrical imaging and distributed temperature sensing methods to characterize surface water-groundwater exchange from a contaminated aquifer to the Columbia River. The array configuration was made of 13 equispaced graphite electrodes at 5 m intervals. Rucker et al. (2011) conducted a waterborne resistivity survey with floating dipole-dipole array along the entire length of the Panama Canal to characterize the types and volumes of sediments and rocks beneath the waterway.

All of these studies agree that submerged electrodes allow for better penetration in the bottom sediments, electrode configuration is strictly connected to the purpose of the survey, and that an optimum a priori choice does not exist. However, from the feasibility point of view, the use of floating arrays appears preferable and exponentially spaced electrodes appear to provide the best depth resolution.

In contrast, references on waterborne magnetic surveys are rare, while towed submerged magnetometer surveys are more usually referred to. Magnetic methods have been used on shallow waters mainly to study magnetic properties of buried structures, to detect the magnetic susceptibility contrasts within the harbor bottom sediments, to map contaminated sediments, and detect ferro-metallic objects buried below the seabed. References on the application of waterborne magnetic surveys on shallow inland waters to image deep geological structures appear lacking.

Boyce et al. (2004) used a marine Overhauser magnetometer towed at a distance of 20 m behind a boat and at a depth of 1–2 m for archaeological surveying. Pozza et al. (2004) used a marine Overhauser magnetometer towed at a distance of 30 m behind a boat at less than 1 m depth for environmental surveying and measured the bathymetry by an echo sounder. Mansoor et al. (2006) acquired data simultaneously from a conductivity meter and a magnetic gradiometer from a paddleboat. The magnetic gradiometer provided information about the maximum spatial extent of a landfill within sensitive marsh area, while the conductivity meter data provided information about the contaminant flux interface from the landfills to the marsh water. For detecting and mapping ferro-metallic objects below the seabed in shallow waters Weiss et al. (2007), presented a system consisting of a magnetic gradiometer and navigation subsystem, both installed on a nonmagnetic catamaran towed by a low-magnetic interference boat, and referenced the data to a stationary-based ground magnetic station. Finally, Embriaco et al. (2009) used a marine magnetic survey, measuring both gradient and total magnetic field (TMF), to search for abandoned magnetic objects at the bottom of a harbor near a highly urbanized area.

Our surveys took advantages of these references and were mainly made with magnetic and electrical systems. The objectives of the present work were to acquire and analyze CVES and magnetic data, combined with GPR, to establish a correlation between the radar reflections and the magnetic and electrical anomalies and using water depth to constrain the magnetic and electric data inversion.

THE SITE

The lake of Candia (45° 19′ N, 7° 54′ E, 226 m a.s.l.) is an intermoraine lake belonging to the morainic amphitheatre of Ivrea, north of Turin, Italy (Figure 1). The magnificent morphology of the Ivrea amphitheatre surrounding the lake is due to the elevated topography and proximity of the plain to its mountain catchment area. The Dora Baltea Valley (the lake is at its southwest corner) is a wide (3400 km^2) and branched valley system with more than 30 main tributary valleys, bounded by some of the highest peaks of the European Alps such as the "Monte Bianco" and the "Cervino," which are not far from the Po Plain. This basin cuts all the main structural systems (from the Sudalpine to the Helvetic System) that form the Alpine range. The Ivrea amphitheatre was built up by the Balteo Glacier, which flowed through the Aosta Valley during the Quaternary period. The Balteo Glacier was on average 3 km wide, around 600 m thick and was spread over 300 km through the Alps. At its maximum expansion, it extended 25 km into the Po plain with a width of about 20 km, reaching today's northern border of the town of Turin.

The lithology is reflected in the petrographic variety of the glacial deposits, dominated by metamorphic silicate rocks and subordinate calcareous clasts. Austroalpine eclogitic mica-schist and gneiss with eclogite and glaucophanite are prevalent. Serpentinite, amphibolite, prasinite, metagabbro, quartzite, calcschist, and marble from the Piemontese Zone are also abundant. Diorite and mafic granulite from the Sudalpine System and many other types of orthogneiss and granitoids, paragneiss, and mica-schist from all the continental systems are also present (Gianotti et al., 2008). Among these rock types those that show relevant magnetic properties (with average susceptibility $k > 29,000 \times 10^{-6}$) are the serpentinized peridotites, the main gabbro-like rocks and some mafic rocks (Belluso et al., 1990). A borehole (Alice Superiore borehole) drilled about 20 km NNW of Candia Lake (Figure 1) penetrated similar stratigraphic architecture and provides more detailed information about the top 80 m of the stratigraphic section (Figure 2). The subsurface consists dominantly of marginal and subglacial till, fluvioglacial, and proglacial deposits varying from mud-fill dense gravel to coarse gravel with boulders with coarse sand and blue mud in the lower parts of the stratigraphic section. A palustrine gyttja layer, made of peaty brown clay, represents the interstadial episode between the two glacial events.

The Candia Lake has a surface area of about 1.52 km^2, a perimeter of about 5.5 km, and an estimated volume of about 7.2 Mm^3 with a maximum depth of about 7.5 m. The lake remained after the Riss Glaciation receded (about 150,000 YBP), settled in a plain that was eroded by the advancing glacier, and then refilled to a far lower extent by the glacial deposits of the glacier retreat. According to Gianotti et al. (2008), the Candia Lake lies on the Piverone alloformation (Late Pleistocene) above the Serra alloformation (end of the Middle Pleistocene), each one referable to a different glacial episode. Until about 50 years ago, before an eutrophication process took place, the white gravels of the lake bottom and the fresh water columns rising up from underwater springs were visible from the lake surface. Today, the silts and the vegetation prevent the view of the lake bottom. The lake has neither affluent nor effluent, but a small ditch used sometimes for irrigation. Water recharge is from rains and underwater springs.

Figure 1. Geographical location of the site.

DATA ACQUISITION

On 17 May 2010, we acquired 21 magnetic profiles on the Candia Lake, with a total length of 37.7 km and about 17,000 TMF measurements (Figure 3a). The survey resulted in an average spacing between the readings of about 2.2 m along the profiles that we planned to be, on average, 30 m apart (Figure 3a). The acquisition rate was 1 reading/second and it took from 10 to 15 minutes to acquire each profile. A GEM GSM19V Overhauser proton magnetometer was placed 2 m apart from a GPS system "Topcon GMS2" on a rubber dinghy pulled about 20 m behind the sailing boat.

To perform a waterborne CVES survey, a georesistivimeter able to deliver a spatial sampling adequate with respect to both the boat

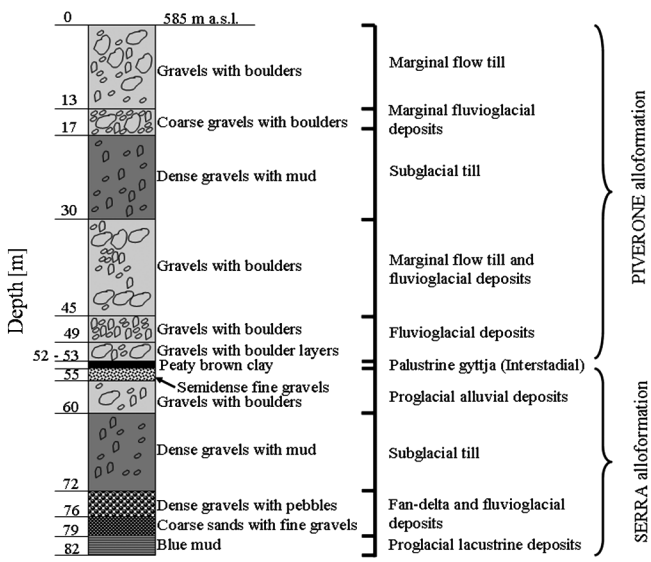

Figure 2. Stratigraphic log of the geological environment.

speed and the required VES density, is needed. Today this could be accomplished with DC or AC instrument. The AC instruments have the advantage that the electrode polarization is avoided and, in case of a relevant number of connected electrodes, the overall acquisition time is sensibly reduced.

On 17 June 2010, we acquired an electrical survey consisting of four CVES profiles (Figure 3b) near the shore of Candia lake with a total length of about 3.6 km and, on average, one VES every 1.5 m. We used a Pasi Polares georesistivimeter which, given the expected water depths and resistivities, was suitable with respect to both output power and acquisition rate. We set the georesistivimeter to drive a sinusoidal potential between the current electrodes at 114 Hz. On average, the peak current amplitude we read was 350 mA. The georesistivimeter was connected to a GPS system Topcon GMS2 to get the spatial position of the tracks. The array was made from two current electrodes near the boat, followed by seven gold-plated potential electrodes. To give the current electrodes a large surface area, yet preserve an acceptable point source condition, we designed them with radial fins, while the potential electrodes were simple cylinders (Figure 4a). The current electrodes, the nearest to the boat, were 16 m apart; the first potential electrode was 0.5 m beyond the farther current electrode. The potential dipoles had exponentially (integer power of 2) increasing separations of 0.5, 1, 2, 4, 8, 16 m (Figure 4b). The towed cable floated on the lake surface because we tied empty plastic bottles near the electrodes that were fully submerged. The cable was kept stretched by a floating anchor fixed at its end.

GPR measurements were acquired contemporaneously with magnetic and resistivity surveys. We used a K2 IDS georadar with a Subecho-70 monostatic transceiver antenna, with peak frequency at 89 MHz. We placed the antenna at the bottom of our fiber-reinforced plastic boat; a Garmin GPS60, connected to the K2 unit and nearby the antenna, tracked the GPR traces. We acquired an average of 10 trace/m, and the trace length was 600 ns with a sampling frequency of 1.7 GHz. Neither filters nor gains were applied during the acquisition.

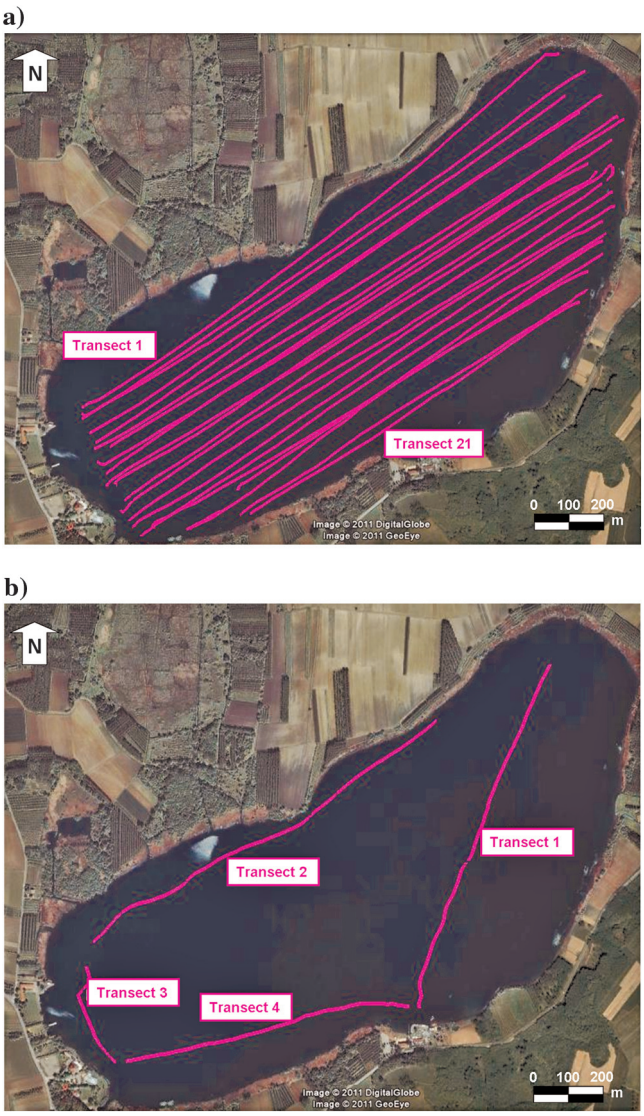

Figure 3. (a) Magnetic survey transects; (b) Electrical survey transects.

DATA PROCESSING AND INVERSION

In this section, we describe the data processing and inversion techniques used for the different methodologies. We paid particular attention to the strategies implemented in the inversion of magnetic and CVES surveys, while standard procedures are used with respect to GPR data.

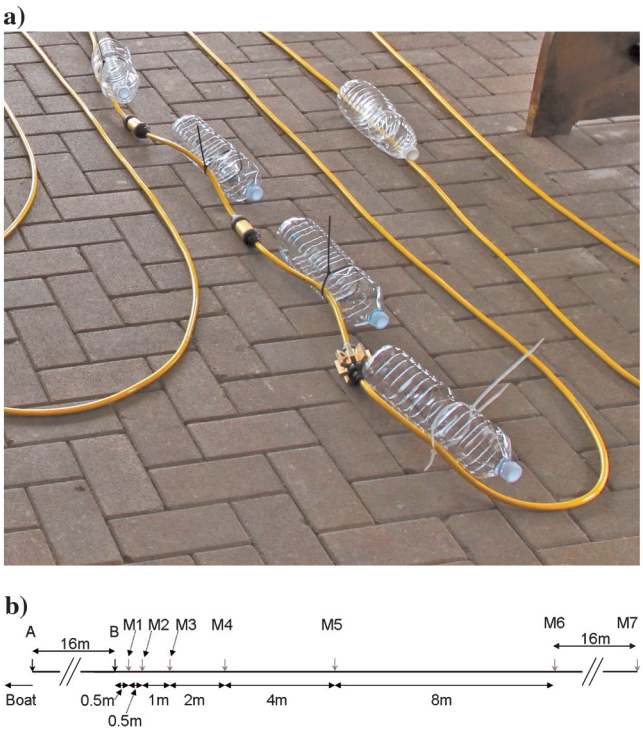

Figure 4. Electrical cable: (a) a current electrode with radial fins and cylindrical potential electrodes. Empty bottles kept the cable floating; (b) electrodes geometry.

GPR

We processed all the GPR profiles with the software Reflexw according to the following steps in sequential order: (1) corrected for the direct arrival delay and applied a dewow filter to eliminate a very low frequency trend; (2) band-pass filtered with a Butterworth fourth order filter from 20 to 190 MHz to attenuate both low and high frequency noise; (3) resampled the traces to obtain a trace interval of 0.2 m; (4) removed background clutter with a spatial high-pass filter; (5) applied a divergence compensation to recover the amplitude attenuation due to the geometrical spreading and restore the strength of reflections from bottom materials; (6) enhanced the continuity of the reflectors by applying a horizontal running average over 11 traces that roughly corresponds to a low pass filter that, giving the spatial sampling interval, attenuates the wavelengths shorter than 2 m, and finally, (7) picked the first bottom reflection to estimate the bathymetry of the lake. We used the picks to mute the upper parts of the radargrams related to water.

Magnetic survey

For the magnetic survey, we first corrected the TMF readings for the diurnal variation according to the data from the INGV geomagnetic observatory of Castello Tesino (46° 03′ N, 11° 39′ E, 1175 m. a.s.l.) north of Trento (Italy). A TMF map was then computed (Figure 5) by adopting a triangular interpolation process. To obtain more quantitative information on the depth, size and susceptibility of the causative bodies of the magnetic anomalies visible at the SE side, we performed a 2D inversion of the three profiles shown in Figure 5, even though the magnetic map around the profiles shows a magnetic body can be defined to be 2D when its strike length in the direction perpendicular to the profile is at least 10 times its width (Telford et al., 1990). Therefore, we consider the inversion results only as rough estimates of the size and depth of magnetic anomaly sources.

We adopted a 2D constrained, compact, magnetic inversion to invert the profiles. Our starting point was a software (Stocco et al., 2009) developed from the original approach of Last and Kubik (1983). The code has been modified so that the thickness of the water layer drawn from the GPR bathymetry could be used as a constraint.

Following Bhattacharyya (1964) the water/soil volume beneath the magnetic profile can be split into Q rectangular prisms that extend infinitely orthogonally to the profile direction, with X_j the unknown magnetic susceptibility of the jth prism. Using the formula reported in Telford et al. (1990), we were able to calculate at each of the W measuring points along the magnetic profile the value t_i of the TMF intensity caused by the magnetic fields of all the prisms, such that

$$t_i = F \sum_{j=1}^{Q} K_{i,j} \chi_j, \tag{1}$$

where F is the local Earth magnetic field intensity and $K_{i,j}$ represents a known geometrical function relating the size and the distance of the prism j from the measurement point i (details in Stocco et al., 2009). Equation 1, neglecting F, can also be written in matrix form as

$$\boldsymbol{t} = \boldsymbol{K}\boldsymbol{\chi}, \tag{2}$$

where $\mathbf{t}$ is a column vector with W rows, $\boldsymbol{K}$ is a $W \times Q$ kernel matrix and $\boldsymbol{\chi}$ is a column vector with Q rows.

In waterborne surveys, however, some of the prisms under the magnetic profile are constituted by water and the susceptibilities referring to this subset of prisms $\{\tilde{\chi}\}$: $\{\tilde{\chi}\} \subset \{\chi\}$ is known. We then used our knowledge of the magnetic susceptibility for these prisms to force the inversion to "explain" the magnetic anomalies only with bodies within the sediments.

We performed a preliminary multiplication on the right side of equation 2 only for the $\tilde{\chi}$ values, and obtained a vector $\tilde{\mathbf{t}}$ related to the influence of the water layer in the measurements such that

$$\tilde{\boldsymbol{t}} = \tilde{\boldsymbol{K}}\tilde{\boldsymbol{\chi}}, \tag{3}$$

where, at this step, $\tilde{\boldsymbol{K}}$ is the subset of the kernel matrix which considers only prisms above the lake bottom. In a second step, we considered only prisms under the lake bottom and inverted:

$$(\boldsymbol{t} - \tilde{\boldsymbol{t}}) = \underset{\sim}{\boldsymbol{K}}\,\underset{\sim}{\boldsymbol{\chi}} \tag{4}$$

where $(\boldsymbol{t} - \tilde{\boldsymbol{t}})$ becomes the experimental data stripped of the water effect, and $\underset{\sim}{\boldsymbol{K}}$ and $\underset{\sim}{\boldsymbol{\chi}}$ are, respectively, the kernel matrix and the unknown susceptibilities relative to the prisms below the lake bottom. In such a way, the values of susceptibilities obtained were assigned only to prisms within the sediments. The principle of the compact inversion used (Last and Kubik, 1983) involves minimizing the area of the source body (maximize its compactness). The problem is slightly underdetermined and it can be profitably solved using the weighted — damped least-squares inversion (Stocco et al., 2009).

We compare the inversion of a synthetic dataset (Figure 6a) with the proposed approach to an inversion performed using the same algorithm but not accounting for the presence of water (i.e., inverting directly $\boldsymbol{t}$). In both inverted data, (top of Figure 6b and 6c) a good fitting with synthetic data can be observed. However, the reconstructed models are significantly different in terms of position of the anomalies and susceptibility values. Taking into account the water bathymetry and its influence on the measurements drastically

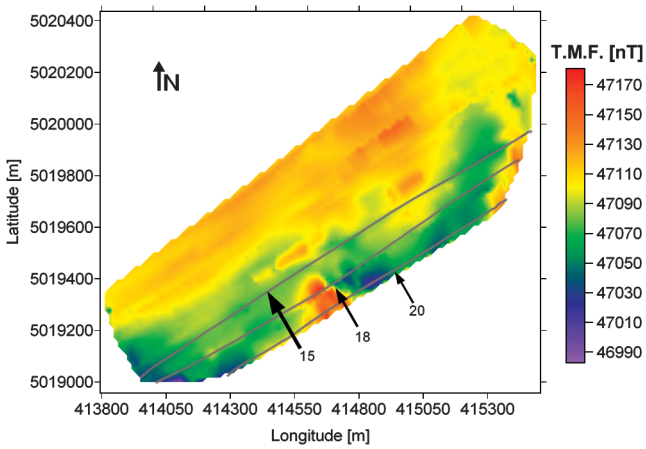

Figure 5. TMF magnetic map of Candia lake. The three profiles where 2D inversions are performed are shown.

improves the correspondence of the final result with the correct model. This is particularly true with respect to the identification of the correct depth and position of the anomalies. This effect is clearly more evident when the anomaly dimensions compare to the water thickness or are in the shallow subsurface (e.g., in archaeological studies). Similar conclusions have been reached by others (e.g., Boyce et al., 2004; Faccioni et al., 2003; Pozza et al., 2004) even if with partially different approaches.

The use of this inversion approach also allowed to partially overcome the limitations in the number of unknowns (X_j of the prisms) with respect to the number of equations (magnetic field measurements). A compromise, based on the number of prisms used in the inversion, between resolution and compactness is required. The number of unknowns should be limited proportionally to the experimental values, while smaller prism dimensions (i.e., greater number of prisms) are required at least on top of the domain to better fit the lake bathymetry.

We therefore used two prism sizing criteria. We adopted a more refined subdivision of the water volume (which influences the number and typology of elements in $\tilde{\boldsymbol{K}}$) by using prisms with a constant reduced height (0.5 m) until the bottom of the lake is reached (Figure 7). Below the lake bottom the prisms ($\underset{\sim}{\boldsymbol{K}}$) have an increasing height (geometrical progression) to account for the decay of the magnetic field and to reach a satisfying investigation depth (Figure 7). The heights of the first elements under the lake bottom are determined by considering the actual value of the progression starting from the water surface. The horizontal extent of the prisms in both domains is instead constant and equal to about $1/100$ of the length of the profile. An example of the results obtainable by means of this last approach is shown in Figure 8, based on the synthetic dataset of Figure 6a. As for the experimental data presented later, the result of the inversion is depicted with a contour map of the prisms pertaining only to lake sediments. An even better

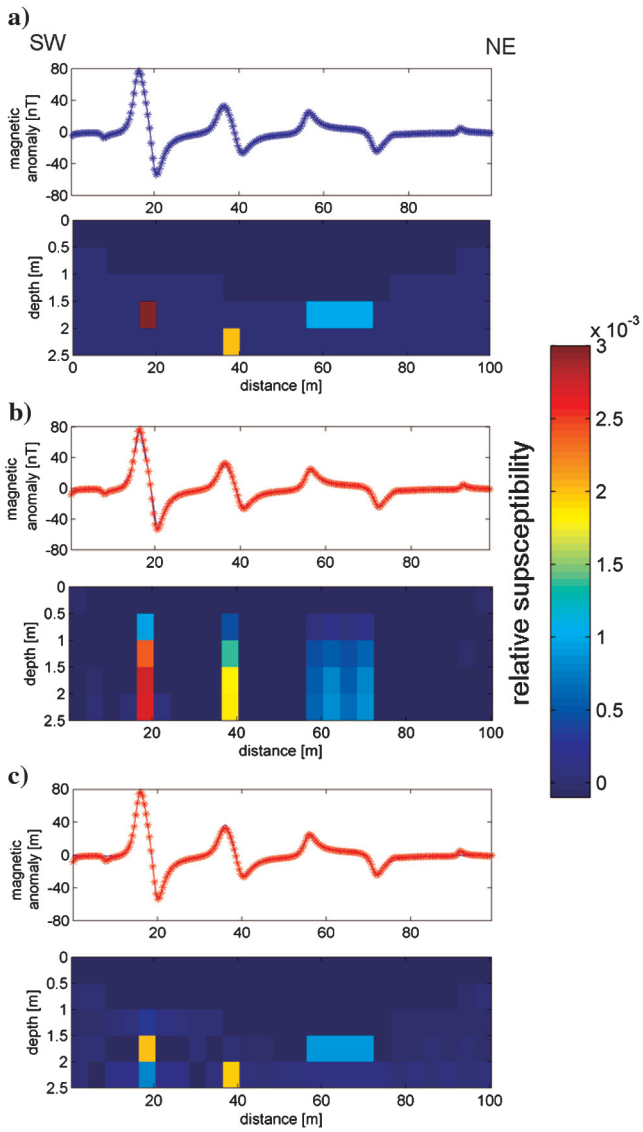

Figure 6. Inversion of synthetic magnetic data: (a) synthetic model; (b) inverted model not accounting for the water bathymetry; (c) inverted model accounting for water bathymetry.

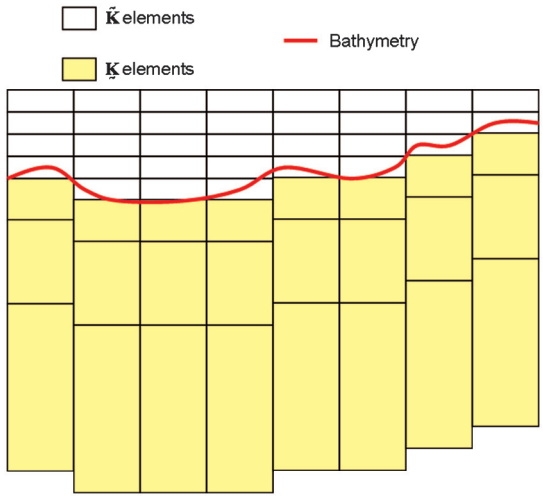

Figure 7. Different definition of block heights in the two kernels.

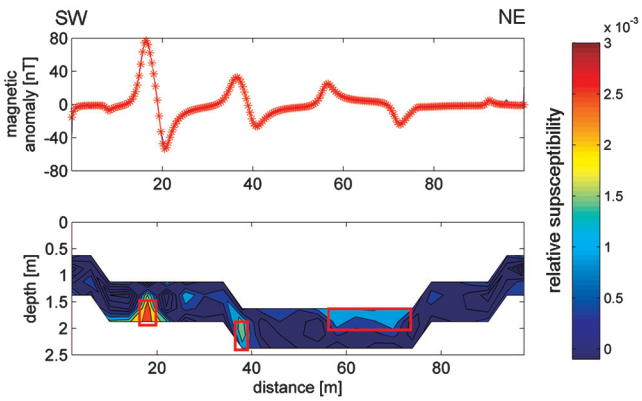

Figure 8. Inversion of synthetic data: contour map of the inverted model accounting for water bathymetry with evidence of the synthetic anomalous bodies.

correspondence with the synthetic model was obtained in terms of relative susceptibility values.

CVES survey

Before inverting the data we performed some statistical processing to evaluate the homogeneity of water resistivity and the data variability with depth. We calculated mean, standard deviation, median, minimum, and maximum of the apparent resistivity for each of the six dipoles, over 2290 VES curves. From the results presented in Figure 9, it is clear that the first three dipoles likely investigate the water which can be safely considered as electrically uniform, with values ranging from 60 to 65 Ωm. The $\pm 1\sigma$ bars pertaining to these dipoles are in fact nearly invisible. On the other hand, from the fourth to the farthest dipole the standard deviation bars increase, as well as the dispersion of the data, as shown by the diverging minimum and maximum curves. Further information can be drawn from the bending, toward lower resistivity values, of the mean and median curves with the increasing of dipole spacing. These data are expected to give information about the sediments so that, from this trend, it can be inferred that most of the sediments underneath the profiles have a resistivity lower than the one of water and only a small fraction has a higher resistivity. The standard deviation bars, in fact, although larger than those of the first three dipoles, follow the trend of the mean and median curves.

We inverted CVES data along some profiles using an integrated Laterally Constrained Inversion (LCI) approach. LCI was developed to invert vertical electrical sounding data along a profile by Auken and Christiansen (2004), using a pseudo-2D layered parameterization. The inversion result of LCI performed on electrical soundings is a set of 1D resistivity models in which each separate model corresponds to a sounding (apparent resistivity curve). All the soundings are inverted simultaneously by minimizing a common objective function, which contains the data, the a priori information and the constraints.

The objective function can be expressed as (Auken and Christiansen, 2004):

$$L = \left(\frac{1}{N+M+A} [(\mathbf{d}_{\text{obs}} - g(\mathbf{m}))^T \mathbf{C}_{\text{obs}}^{-1} (\mathbf{d}_{\text{obs}} - g(\mathbf{m}))] + \right.$$
$$\left. + [(-\mathbf{R}_p \mathbf{m})^T \mathbf{C}_{Rp}^{-1} (-\mathbf{R}_p \mathbf{m})] + [(-\mathbf{P}_h \mathbf{m})^T \mathbf{C}_{\mathbf{h-prior}}^{-1} (-\mathbf{P}_h \mathbf{m})] \right)^{\frac{1}{2}} \quad (5)$$

where $\mathbf{m}$ is a vector including the parameters relative to all the spatially distributed 1D resistivity models considered in the inversion process. The vector $\mathbf{m}$ is linked to the observed data set $\mathbf{d}_{\text{obs}}$ (the apparent resistivity curves) with the associated observational covariance matrix $\mathbf{C}_{\text{obs}}$. The quantity N is the total number of data points, M is the total number of the model parameters and A is the number of constraints. The forward problem $g(\mathbf{m})$ is computed with the CR1Dmod algorithm (Ingeman-Nielsen and Baumgartner, 2006) considering homogeneous horizontal layers. The matrix $\mathbf{R}_p$ is the thicknesses and resistivities lateral regularization matrix and $\mathbf{P}_h$ is the regularization matrix relative to the a priori depth. The effectiveness of the $\mathbf{R}_p$ and $\mathbf{P}_h$ matrices depends on the strength of the constraints described in the covariance matrices $\mathbf{C}_{\text{Rp}}$ and $\mathbf{C}_{\text{h-prior}}$ (Auken and Christiansen, 2004; Tarantola, 2005).

Using a deterministic local search approach, the model solution updated at the (n + 1)th iteration can be expressed as:

$$\mathbf{m}_{n+1} = \mathbf{m}_n + ([\mathbf{G}^T \mathbf{C}_{\text{obs}}^{-1} \mathbf{G} + \mathbf{R}_p^T \mathbf{C}_{\text{Rp}}^{-1} \mathbf{R}_p + \mathbf{P}_h^T \mathbf{C}_{\text{h-prior}}^{-1} \mathbf{P}_h + \lambda \mathbf{I}]^{-1}$$
$$\cdot [\mathbf{G}^T \mathbf{C}_{\text{obs}}^{-1} (\mathbf{d}_{\text{obs}} - \mathbf{g}(\mathbf{m}_n)) + \mathbf{R}_p^T \mathbf{C}_{\text{Rp}}^{-1} (-\mathbf{R}_p \mathbf{m}_n)$$
$$+ \mathbf{P}_h \mathbf{C}_{\text{h-prior}}^{-1} (\mathbf{h}_{\text{prior}} - \mathbf{P}_h \mathbf{m}_n)]), \quad (6)$$

where the Jacobian $\mathbf{G}$ represents the sensitivity matrix. Considering the nonlinearity of the problem, the iterative procedure is stabilized by the Marquart damping parameter λ (Marquart, 1963). At each iteration the global misfit of all the soundings is evaluated (Auken and Christiansen, 2004). The convergence of the inversion is obtained when the misfit reduction between the current iteration and the previous one is smaller than a user-defined threshold or when a predetermined number of iterations has been reached.

The lateral constraints can be applied to neighboring resistivity models by imposing that thickness and resistivity of the same layer must be similar. The degree of similarity is ruled by the strength of the constraints that are set in the $\mathbf{C}_{\text{Rp}}$ matrix according to the expected lateral variability; if lateral variability is small, we can set a medium or strong constraint and vice versa. Through the lateral constraints, information from one electro-stratigraphic section spreads to the neighboring ones, producing a smoothly varying 2D section.

We used the GPR data to constrain the lake bottom depth in the LCI of the experimental apparent resistivity curves. We present results relative to profile four (Figure 3b). We computed average VES curves to obtain a mean and a standard deviation value of apparent resistivity and to reduce the number of VES and the computational time of the inversion (the original VES spacing was of 1.5 m along each profile). We refer to the AB spacing to select the averaging length. Since the AB spacing was 16 m, we averaged the VES curves by applying a nonoverlapping moving window over a length of 15 m; we considered this the lateral resolution within the profile. According to the selected window length we carried out the average over 10 curves. Four of these averaged curves are shown in Figure 10. Each averaged curve provides an apparent resistivity curve that approximates measured data and is located in the center of the adopted window. We then considered the standard deviation, calculated within the moving window, to be the data uncertainty for the observational covariance matrix $\mathbf{C}_{\text{obs}}$. For CVES profile 4 (presented in the following section) we obtained 65 averaged apparent resistivity curves.

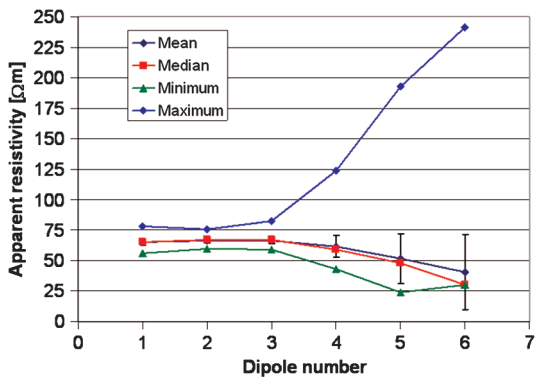

Figure 9. Statistics over 2290 measured apparent resistivities. The error bars correspond to $\pm 1\sigma(\rho_{\text{app}})$. Dipole number one is the potential dipole nearest to the boat (M1-M2 in Figure 4b), dipole number six is the farthest (M6-M7 in Figure 4b).

RESULTS

The GPR survey is mainly a subsidiary tool for the other methodologies adopted. From the processed GPR data we obtained a bathymetry map of the lake (Figure 11). The depth values are gridded with triangular interpolation of a 30 × 30 m mesh. The results pertaining to the other two survey techniques are discussed in more details below.

Magnetic survey

The magnetic map (Figure 5) highlights three distinct areas of relatively uniform magnetic field that could be related to different geological settings. The overall bottom of the lake appears generally divided into two domains (on the northwest side and on the southeast side). This distinction appears consistent with the mechanism of formation of the lake and of the plain sediments because the plain was refilled by proglacial alluvial deposits during glacier retreat and by late lacustrine deposits after the formation of the moraine ridges. As the lake is at the limit between the moraine material and the refilled material (Figure 12), the separation between these two zones is evidenced by different values of the magnetic field over the lake. The higher intensity of magnetic field on the north-northeast side of the map could also be partially related to a secondary glacial terrace that formed after the main glacial retreat, after the formation of the main moraine ridge, and which also helped the lake formation. Moreover, a relatively compact high intensity magnetic anomaly occurs in the south of the map. This anomaly could be related to a protruding moraine foot originated from the main ridges of the moraine. Given its higher magnetic field, it may contain boulders or blocks with greater dimensions with respect to the surrounding deposits (see also the single profile inversions below).

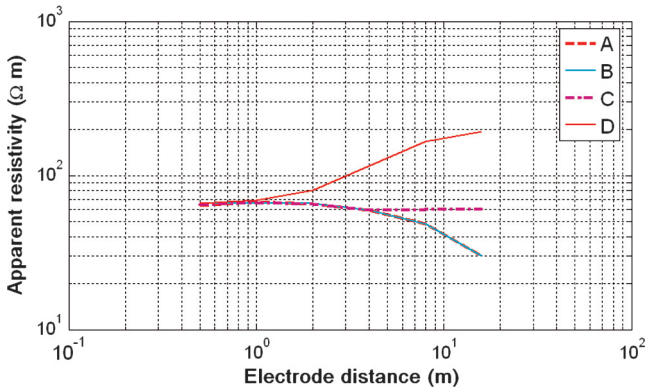

Figure 10. Comparison of four of the 65 apparent resistivity curves extracted along profile four; curves locations along the profile are reported in Figure 16. Electrode distance is assumed to be the distance between the second current electrode and the first potential electrode of each dipole.

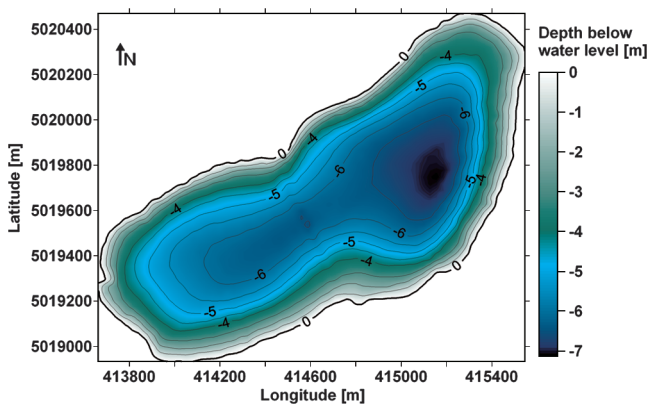

Figure 11. Bathymetric map obtained from GPR data.

We show three examples of magnetic profile inversion corresponding to profiles 15, 18, and 20 (Figures 13, 14, and 15). The 2D condition is not completely satisfied for profiles 18 and 20 (Figure 5) because these profiles cut the main anomaly in the map. The anomaly has indeed a limited lateral extension so that possible 3D effects could influence the results. This is particularly true for profile 20, which is located near the limit of the map. It is, however, probable that the anomaly also continues to the south of the map, outside of the lake border, given the postulated continuity of the moraine. Nevertheless, distinctive features can be noted in the three inverted profiles and can be correlated to the results of GPR surveys.

Along profile 15 (Figure 13) a relatively uniform susceptibility distribution appears coherently with the uniform magnetic field observed. In profile 18 (Figure 14), a distinctive anomaly occurs between 500 and 700 m. The location of the anomaly is highly coherent with a strong reflector in the radargram that extends in the same horizontal location and at a depth that roughly matches the top of the anomaly obtained after the profile inversion. A similar anomaly is observed along profile 20 (Figure 15) although, along this last profile, the main anomaly appears wider (from 300 to 600 m). Moreover, some reduced secondary irregularities on the top of the main anomaly are observed, which correspond to the short wavelength oscillations in the data. We interpret this main anomaly to be part of a moraine foot (Figure 12). This interpretation is supported by a morphological feature of the bathymetry map (Figure 11) because near the central-south part of the lake shore, the bathymetric lines show a pronounced convexity delineating a submerged promontory. Such a structure at its upper part, presents a marked prevalence of pebbles and gravels as also tested by GPR and CVES results.

CVES survey

We show our resistivity results in Figures 16 and 17. In the LCI inversion, we chose a three-layer parameterization to account for three main resistivity units in the sedimentary environment of the Candia Lake: water being the top layer, a middle layer of silt, and gravels representing the deepest layer. We focus on the resistivity results obtained for profile four (located in Figure 3b). The GPR section along this profile highlights a transition zone between about 750 and 900 m, where there are strong reflections from the lake bottom (Figure 16d). These strong reflections are related to gravels that become gradually more superficial from 750 m to 900 m; a key point to be considered while imposing lateral constraints in the inversion of the electrical soundings.

In particular, due to the presence of the aforementioned transition zone, no lateral constraints should be imposed in the middle layer, which represents sediments just beneath the water. However, for the water and deepest sediment layer, a lateral homogeneity of

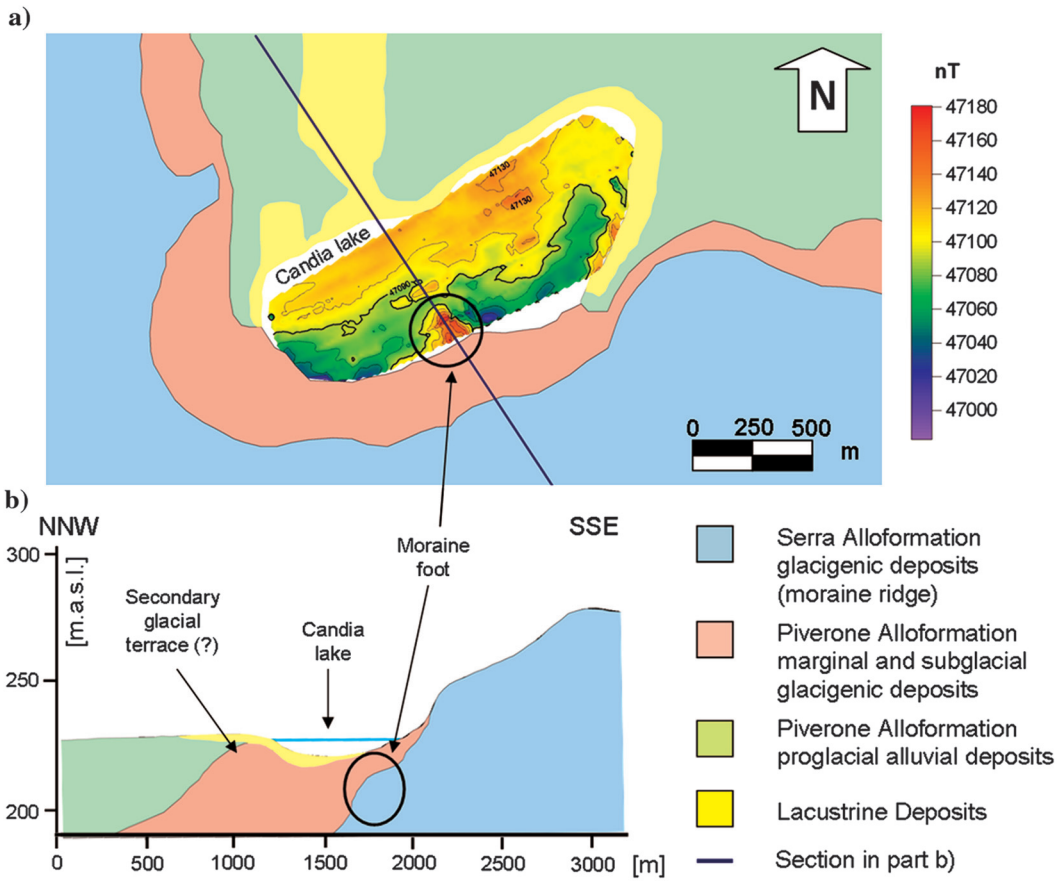

Figure 12. Geological setting of the area: (a) magnetic field strength superimposed upon the geologic map (modified after Gianotti et al., 2008) and (b) geological section cutting the main magnetic anomaly.

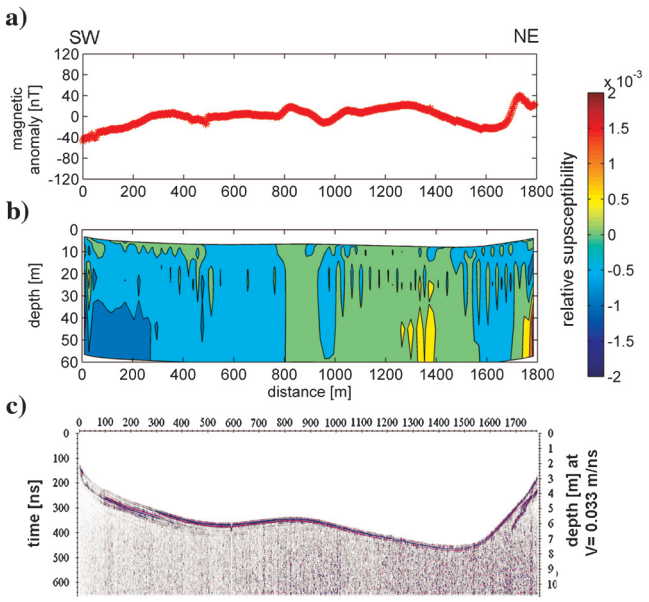

Figure 13. (a) magnetic anomaly and (b) relative susceptibility contour map produced by the 2D inversion of magnetic profile 15, and (c) GPR bathymetry profile.

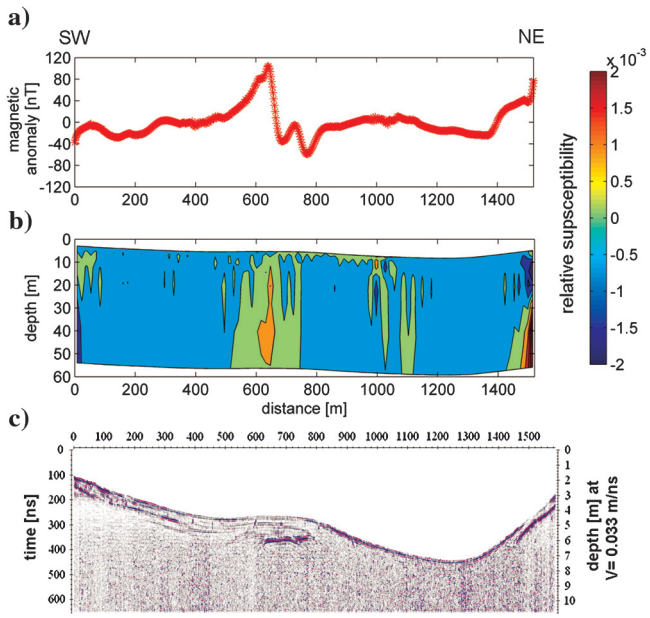

Figure 14. (a) magnetic anomaly and (b) relative susceptibility contour map produced by the 2D inversion of magnetic profile 18, and (c) GPR bathymetry profile.

resistivities is reasonably expected and thus smoothness constraints to be considered.

We show the results of three different LCIs performed on profile four varying the degrees of constraint: (a) inversion without any constraint (Figure 16a); (b) inversion imposing a strong constraint on a-priori depth of the water-sediment interface referenced from the GPR bathymetry (Figure 16b); and (c) adding a moderate strength lateral constraint to the resistivity of the first and third layers (Figure 16c). The root mean-square error of the differences between the field data and calculated data of the final inverted model varied between 3.8% and 6.9% for all inversions.

The inclusion of a priori GPR information about lake bottom depth in LCIs (b) and (c) mitigates the nonuniqueness problem of resistivity data inversion by definition, leading to more stable and accurate results with respect to the unconstrained inversion (a). In LCI constraint (c), lateral smoothness constraints are not imposed to the second layer to take into account the possible resistivity discontinuity which is related to the aforementioned transition zone.

We fixed our constraints by requiring that modeled data $g(\boldsymbol{m})$ must lie in the confidence interval given by three times the data uncertainty above and below the experimental data. All modeled data that lie in this interval are equivalent and acceptable, whereas modeled data that exceed it artificially smooth the results, and are not acceptable. LCI constraint (c) respected the confidence interval, as well as LCI constraint (b) (Figure 17), but it contained a lateral smoothing in the first and third layers that enforced a reasonable and expected lateral continuity of resistivities.

The results obtained for the three cases (Figure 16) show that GPR information, introduced in the LCI in terms of a-priori information with the strong constraint (b), drives the positioning of the water-sediment interface. Applying suitable lateral constraints on resistivities gives more smoothed results (c). The final electrical section (Figure 16c) correlates well with the GPR section (Figure 16d). The apparent resistivity model also defines a resistivity contrast associated with the gravel — silt interface, as inferred from GPR data. In particular, in the inverted electrical section, higher apparent resistivity values (about 250 Ωm) in the east part highlight the presence of gravel sediments, while westward lower resistivity values (ranging from about 35 to 45 Ωm) correspond to silts. The mean water resistivity evaluated from the inversions is about 60 Ωm. In this respect, we emphasize that no a-priori information about water salinity/quality were used in the LCI as a-priori input.

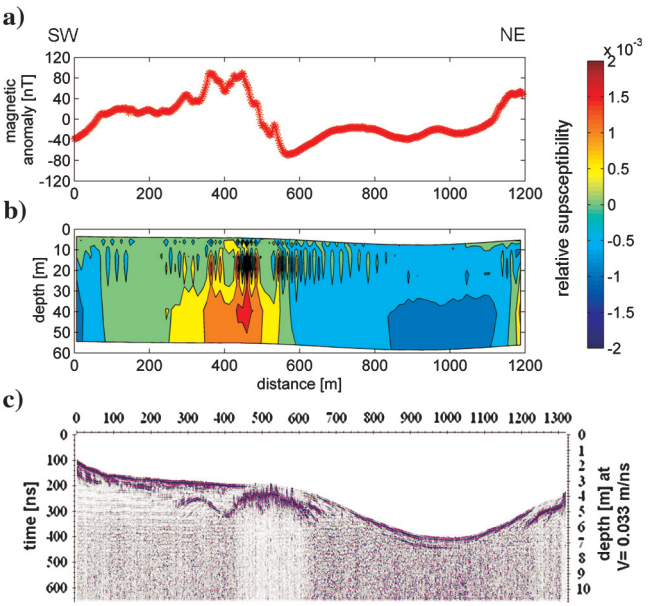

Figure 15. (a) magnetic anomaly and (b) relative susceptibility contour map produced by the 2D inversion of magnetic profile 20, and (c) GPR bathymetry profile.

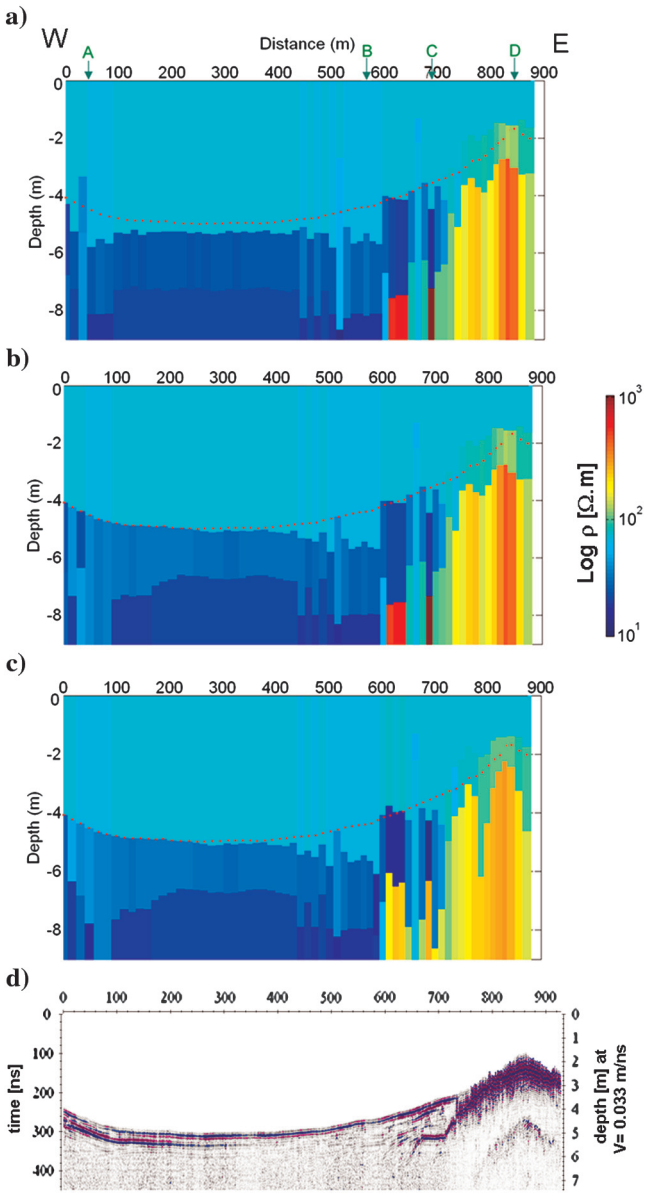

Figure 16. Resistivity LCI inversion of profile four with (a) no constraints (b) strong constraint on radar bathymetry; (c) strong constraint on radar bathymetry and moderate lateral constraint on resistivity of first and third layers; (d) GPR profile. A, B, C, D refer to the positions of the averaged apparent resistivity curves shown in Figure 10; red dots refer to radar bathymetry.

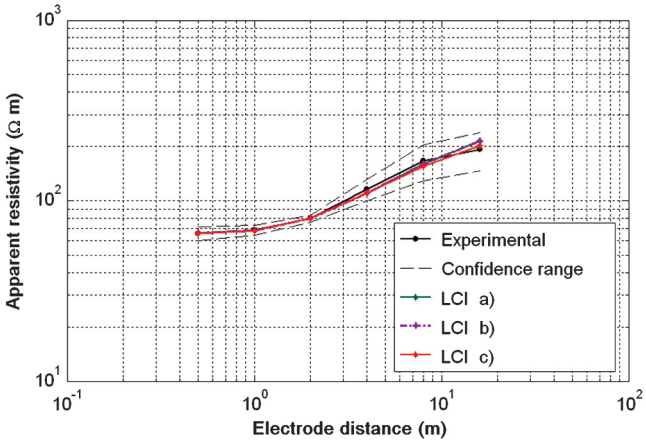

Figure 17. Experimental apparent resistivity curve D of Figure 10 compared with inversion results of the three LCIs: modelled curves (a), (b), and (c) lie in the confidence interval.

CONCLUSIONS

We explored the possibilities of retrieving information on the geological structures beneath a morainic lake by means of waterborne nonseismic methods.

By means of CVES and GPR data we retrieved information on the stratigraphy and on the electrical properties of the superficial bottom sediments while magnetic data helped to elaborate a model of the geological structures under the lake sediments.

We inverted both CVES and magnetic data using GPR data as a constraint, thus increasing the reliability of the geophysical imaging. By means of GPR and CVES we identified a gravel-rich area of the lake bottom that is likely the main hydrological window connecting surface to underground waters. Below this area we identify, from the geomagnetic data, a deep foot of the moraine that bulges into the lake perimeter and is likely topped by the gravels identified with the other two methods.

The methodologies we used had some limitations. Due to the sediment resistivities, neither GPR nor CVES had enough penetration to detail bedding while magnetic had not enough resolution.

A multimethods approach including seismic or acoustic subbottom surveys, providing superficial sediments have low reflectivity, with techniques mutually constrained and integrated, could give a complete set of information on the sediment bedding and bedrock structures.

ACKNOWLEDGMENTS

The authors would like to thank the "Ente Parco naturale di interesse provinciale del Lago di Candia" for the permission to work on the lake and publish the results. Thanks are also due to Alessandro Arato, Mariantonia Zappone, and Diego Franco for their help in collecting and processing data, and to Dr. Franco Gianotti for the valuable discussions on the geology of the lake surroundings. We would also like to thank Dr. Antonio Meloni of INGV for supplying the data from the geomagnetic observatory of Campo Tesino and Dr. Daniele Boiero for valuable discussion on laterally constrained inversion issue. Many thanks also to David Allen, Steve Arcone, and Nasser Mansoor for their detailed and helpful review. This study has been funded by MIUR GRANT 2007ET8X4C_002: "GeoElectromagnetic Methods for Mapping River Sediments (GEMMARS)" within the project "Groundwater control, protection and management. The contribution of innovative geophysical methods." The development of the Polares has been partially realized within the SoilCAM project, funded in the 7th Framework Programme, call ENV.2007.3.1.2.2 by the European Union.

REFERENCES

Allen, D., and N. Merrick, 2007, Robust 1D inversion of large towed geo-electric array datasets used for hydrogeological studies: Exploration Geophysics (Collingwood, Australia), **38**, 50–59, doi: 10.1071/EG07003.

Annan, A. P., and J. L. Davis, 1977, Impulse radar applied to ice thickness measurements and freshwater bathymetry: Report of Activities Part B, Geological Survey of Canada, Paper 7, 7-1b, 63–65.

Apostolopoulos, G., G. Amolochitis, and S. Stamataki, 2006, Marine resistivity measurements for the foundation of lavrion old (1888) French Bridge: Near Surface Conference, Helsinki, P043, 5.

Arcone, S. A., E. F. J. Chacho, and A. J. Delaney, 1992, Short-pulse radar detection of groundwater in the Sagavanirktok River floodplain in early spring: Water Resources Research, **28**, 2925–2936, doi: 10.1029/92WR01308.

Arcone, S. A., D. Finnegan, and G. Boitnott, 2010, GPR characterization of a lacustrine UXO site: Geophysics, **75**, no. 4, WA221–WA239, doi: 10.1190/1.3467782.

Arcone, S. A., D. Finnegan, and J. E. Laatsch, 2006, Bathymetric and subbottom surveying in shallow and conductive water, Proceedings of the 11th International Conference on Ground Penetrating Radar, on CD-ROM.

Auken, E., and A. V. Christiansen, 2004, Layered and laterally constrained 2d inversion of resistivity data: Geophysics, **69**, 752–761, doi: 10.1190/1.1759461.

Belaval, M., J. W. Lane, D. P. Lesmes, and G. C. Kineke, 2003, Continuous-resistivity profiling for coastal ground water investigations: Three case studies: Symposium on the Application of Geophysics to Engineering and Environmental Problems.

Belluso, E., G. Biino, and R. Lanza, 1990, New data on the rock magnetism in the Ivrea-Verbano zone (Northern Italy) and its relationships to the magnatic anomalies: Tectonophysics, **182**, 79–89, doi: 10.1016/0040-1951(90)90343-7.

Bhattacharyya, B. K., 1964, Magnetic anomalies due to prism-shaped bodies with arbitrary polarization: Geophysics, **29**, 517–531, doi: 10.1190/1.1439386.

Boyce, J. I., E. G. Reinhardt, A. Raban, and M. R. Pozza, 2004, Marine magnetic survey of a submerged Roman Harbour, Caesarea Maritima, Israel: The International Journal of Nautical Archaeology, **33**, no. 1, 122–136, doi: 10.1111/j.1095-9270.2004.00010.x.

Bradbury, K. R., and R. W. Taylor, 1984, Determination of the hydrogeological properties of lakebeds using offshore geophysical surveys: Ground Water, **22**, 690–695, doi: 10.1111/j.1745-6584.1984.tb01437.x.

Butler, K. E., 2009, Trends in waterborne electrical and EM induction methods for high resolution sub-bottom imaging: Near Surface Geophysics, **7**, no. 4, 241–246, doi: 10.3997/1873-0604.2009002.

Delaney, A. J., P. V. Sellmann, and S. A. Arcone, 1992, Sub-bottom profiling: A comparison of short-pulse radar and acoustic data: Proceedings of the 4th International Conference on Ground Penetrating Radar, 149–157.

Embriaco, D., C. Carmisciano, F. Caratori Tontini, P. Stefanelli, L. Cocchi, M. Locritani, and M. De Marte, 2009, Environmental magneto-gradiometric marine survey in a highly anthropic noisy area: Annals of Geophysics, **52**, no. 5, 459–467.

Faccioni, O., F. C. Tontini, P. Stefanelli, C. Carmisciano, L. Cocchi, and I. Giori, 2003, A topographic surface reduction of aeromagnetic anomaly field over the Trrenian sea area (Italy): Marine Geophysical Researches, **24**, no. 3-4, 265–267.

Gianotti, F., G. M. Forno, S. Ivy-Ochs, and P. Kubik, 2008, New chronological and stratigraphical data on the Ivrea amphitheatre (Piedmont, NW Italy): Quaternary International: The Journal of the International Union for Quaternary Research, **190**, no. 1, 123–135, doi: 10.1016/j.quaint.2008.03.001.

Ingeman-Nielsen, T., and F. Baumgartner, 2006, CR1Dmod: A matlab program to model 1D complex resistivity effects in electrical and electromagnetic surveys: Computers & Geosciences, 9, **32**, 1411–1419, doi: 10.1016/j.cageo.2006.01.001.

Kelly, B. F. J., D. Allen, K. Ye, and T. Dahlin, 2009, Continuous electrical imaging for mapping aquifer recharge along reaches of the Namoi River in Australia: Near Surface Geophysics, **7**, no. 4, 259–270, doi: 10.3997/1873-0604.2009024.

Kwon, H. S., J. H. Kim, H. Y. Ahn, J. S. Yoon, K. S. Kim, C. K. Jung, S. B. Lee, and T. Uchida, 2005, Delineation of a fault zone beneath a riverbed by an electrical resistivity survey using a floating streamer cable:

Exploration Geophysics (Collingwood, Australia), **36**, 50–58, doi: 10.1071/EG05050.
Lagabrielle, R., and S. Teilhaud, 1981, Prospection de gisements alluvionnaires en site aquatique par profiles continues de résistivité au fond de l'eau: Bulletin de liason des Laboratoires des Ponts et Chaussées, **114**, 17–24, .
Last, B. J., and K. Kubik, 1983, Compact gravity inversion: Geophysics, **48**, 713–721, doi: 10.1190/1.1441501.
Lin, Y. T., C. H. Wu, D. Fratta, and K. J. S. Kung, 2010, An integrated acoustic and electromagnetic wave-based technique to estimate subbottom sediments properties in a freshwater environment: Near Surface Geophysics, **8**, no. 3, 213–221, doi: 10.3997/1873-0604.2010006.
Loke, M. H., and J. W. Lane, 2004, Inversion of data from electrical resistivity imaging surveys in water-covered areas: Exploration Geophysics (Collingwood, Australia), **35**, no. 4, 266–271, doi: 10.1071/EG04266.
Mansoor, N., and L. Slater, 2007, Aquatic electrical resistivity imaging of shallow-water wetlands: Geophysics, **72**, no. 5, F211–F221, doi: 10.1190/1.2750667.
Mansoor, N., L. Slater, F. Artigas, and E. Auken, 2006, High-resolution geophysical characterization of shallow-water wetlands: Geophysics, **71**, no. 4, B101–B109, doi: 10.1190/1.2210307.
Marquart, D., 1963, An algorithm for least squares estimation of nonlinear parameters: SIAM, **11**, no. 2, 431–441, doi: 10.1137/0111030.
Mellett, J. S., 1995, Profiling of ponds and bogs using ground-penetrating radar: Journal of Paleolimnology, **14**, no. 3, 233–240, doi: 10.1007/BF00682425.
Mitchell, N., J. E. Nyquist, L. Toran, D. O. Rosenberry, and J. S. Mikochik, 2008, Electrical resistivity as a tool for identifying geologic heterogeneities which control seepage at Mirror Lake: SAGEEP 2008, 11.
Moorman, B. J., and F. A. Michel, 1997, Bathymetric mapping and subbottom profiling through lake ice with ground-penetrating radar: Journal of Paleolimnology, **18**, no. 1, 61–73, doi: 10.1023/A:1007920816271.
Pozza, M. R., J. I. Boyce, and W. A. Morris, 2004, Lake-based magnetic mapping of contaminated sediment distribution, Hamilton Harbour, Lake Ontario, Canada: Journal of Applied Geophysics, **57**, no. 1, 23–41, doi: 10.1016j.jappgeo.2004.08.005.
Rucker, D. F., G. E. Noonan, and W. J. Greenwood, 2011, Electrical resistivity in support of geological mapping along the Panama Canal: Engineering Geology, **117**, 1-2, 121–133.
Sambuelli, L., S. Bava, C. Calzoni, and S. Stocco, 2010, A GPR survey on a morainic lake northerly Turin (Italy), Proceedings of the 13th International Conference on Ground Penetrating Radar, CD-ROM, 936–941.
Sambuelli, L., and K. E. Butler, 2009, Foreword, in special issue on high resolution geophysics for shallow water: Near Surface Geophysics, **7**, no. 4, 3–4.
Sambuelli, L., C. Calzoni, and M. Pesenti, 2009, Waterborne GPR survey for estimating bottom-sediment variability: A survey on the Po River, Turin, Italy: Geophysics, **74**, no. 4, B95–B102, doi: 10.1190/1.00V7412.
Slater, L., D. Ntarlagiannis, F. Day-Lewis, K. Mwakanyamale, R. Versteeg, A. Ward, C. Strickland, C. Johnson, and J. Lane, 2010, Use of electrical imaging and distributed temperature sensing methods to characterize surface water — groundwater exchange regulating uranium transport at the Hanford 300 Area, Washington: Water Resources Research, **46**, 13.
Stocco, S., A. Godio, and L. Sambuelli, 2009, Modelling and compact inversion of magnetic data: A matlab code: Computers & Geosciences, **35**, no. 10, 2111–2118, doi: 10.1016/j.cageo.2009.04.002.
Tarantola, A., 2005, Inverse problem theory and methods for model parameter estimation: SIAM, 1–342.
Telford, W. M., L. P. Geldart, and R. E. Sheriff, 1990, Applied Geophysics: Cambridge University Press.
Weiss, E., B. Ginzburg, T. R. Cohen, H. Zafrir, R. Alimi, N. Salomonski, and J. Sharvit, 2007, High resolution marine magnetic survey of shallow water littoral area: Sensors, **7**, 1697–1712, doi: 10.3390/s7091697.